Phenol formaldehyde adhesives formulated for advanced X-ray imaging in wood-composite bondlines

Citation	Paris, J. L., Kamke, F. A., Mbachu, R., & Gibson, S. K. (2014). Phenol formaldehyde adhesives formulated for advanced X-ray imaging in wood-composite bondlines. Journal of Materials Science, 49(2), 580-591. doi:10.1007/s10853-013-7738-2
DOI	10.1007/s10853-013-7738-2
Publisher	Springer
Version	Accepted Manuscript
Terms of Use	http://cdss.library.oregonstate.edu/sa-termsofuse

Phenol formaldehyde adhesives formulated for advanced x-ray imaging in wood-composite bondlines

Jesse L. Paris [a,*], Frederick A. Kamke [a,†], Reginald Mbachu [b], Sara Kraushaar Gibson [b]

[a] *Department of Wood Science and Engineering, Wood-Based Composites Center, Oregon State University, Corvallis, 119 Richardson Hall, OR 97330, USA*

[b] *Arclin Chemical,475 28th St., Springfield, OR 97477, USA*

ABSTRACT

A phenol formaldehyde (PF) adhesive was uniformly tagged with iodine such that it yielded sufficient x-ray computed tomography (XCT) gray-scale contrast for material segmentation in reconstructed wood-composite bondlines. Typically, untagged adhesives are organic and have a similar solid state density as wood cell-walls, and therefore cannot be segmented quantitatively in XCT data. The iodinated PF development involved analysis and comparison of three trial adhesives containing rubidium, bromine or iodine. Adhesive tag efficacy was measured in terms of x-ray absorption contrast enhancement and tag uniformity along the adhesive polymers. Cured adhesive density, tag-element and concentration were each found to significantly impact XCT contrast results, which in turn agreed with theoretical x-ray attenuation predictions for each resin. Ion chromatography confirmed the absence of free iodide in the liquid PF prior to bonding, and fluorescence microscopy and energy dispersive spectroscopy (EDS) showed that iodine tags remained associated with the cured adhesive polymers. XCT and EDS results also demonstrated that when contrast agents are simply mixed into resins, rather than attached to the polymer chains, they are free to migrate independent of the penetrating adhesives during bonding. This then can cause complications with quantitative segmentation and analyses. The iodinated PF yielded consistent and uniform XCT gray-scale contrast; its formulation could be adjusted for other viscosity or molecular weight distribution, which would affect its penetration behavior.

Key words:
x-ray computed tomography, wood-composites, wood-adhesives, x-ray contrast, energy dispersive spectroscopy, adhesive penetration

[*] Corresponding author. Tel.: +804 338 4383; Fax +541 737 3385
E-mail address: Jesse.Paris@oregonstate.edu (J.L. Paris)
[†] Secondary corresponding author. Tel.: +541 737 8422; Fax +541 737 3385
E-mail address: fred.kamke@oregonstate.edu (F.A. Kamke)

1 Introduction

Reducing solid wood into smaller components and reforming them into engineered composite materials via adhesive bonding, extends the resource and randomizes natural variation affording composites more uniform material properties [1]. Adhesive penetration and subsequent solidification in the porous wood structures increase the surface area over which the intermolecular chemical interactions governing wood adhesion effectively operate, and mechanically interlock the adherends [2]. Additionally, penetration transfers joint-stresses, past inherent surface irregularities and machining defects, into undamaged wood cells which is believed to enhance bond strength, toughness, and durability [3,4,1,5]. However, debate remains as to the quantitative role of adhesive penetration, and what is considered an optimum or sufficient level, in composite joint assemblies. These issues are difficult to ascertain, in part, because adhesive penetration is commonly assessed with various two dimensional (2D) microscopy techniques which are both destructive to the composite specimen and neglect the true three dimensional (3D) bond [6].

X-ray computed tomography (XCT) is non-destructive and provides 3D images for the internal structures of materials. XCT is an extremely valuable analytical tool in medical, mechanical engineering and materials-science research disciplines, and within the past decade has grown in application to wood and wood-composites [7-16]. While XCT has yielded detailed, micro-scale 3D wood anatomy data [17,18,12,14,19,20], tracking adhesive infiltration has proven difficult with typical adsorption contrast tomography.

Absorption contrast is achieved when neighboring materials have different linear attenuation coefficients, μ. This value relates to the mean free path of a penetrating x-ray photon in a material before being absorbed or scattered. With highly coherent, mono-energetic x-ray photons, as is the case with synchrotron radiation sources, μ is easily calculated according to Beer-Lambert's law as the ratio of the transmitted, I, to initial, I_0, radiation intensity through the material's thickness, d [21,22].

$$I / I_0 = \exp^{(-\mu d)}$$

The value of the linear attenuation coefficient is a function of both the material's elemental composition and density; dense materials and those with high atomic number (Z), contain more electrons per unit volume, and thus have higher μ values [7]. Wood and phenol formaldehyde (PF) adhesives are both organic, being primarily comprised of carbon, hydrogen and oxygen; moreover, once cured, the PF density is similar to that of the wood cell-wall at approximately 1.5 g/cm³. Therefore, wood-composite XCT reconstructions often show minimal gray-scale intensity differences between the wood and adhesive phases at micron-scale resolutions, which makes quantitative material segmentation nearly impossible [15,11]. Several

researchers have attempted to overcome these problems by tagging the adhesive, or matrix phase in the case of wood-plastic composites, with various heavy metal contrast agents [9,13,15,23,24,16]; however two significant complications have been identified from these tagging methods. First, phase separation and tag mobility is suspect. If tag compounds are not directly attached to the adhesive pre-polymers, they are free to migrate [11,15]. Such tag mobility can result in agglomeration, and thus differences in localized attenuation values within the resin phase [13,23,24]. Second, if tags do remain associated with the adhesive phase, it is often unclear how uniform they are distributed along the polymer chains. PF adhesives are typically poly-disperse systems with complex reaction schemes during formulation; one would not expect long and short polymer chains to be tagged to the same degree. This too might cause variations in adhesive attenuation coefficients, as resin mobility and penetration depth are, in part, a function of molecular weight. Both complications reduce confidence and accuracy when segmenting wood-composite micro-XCT data into the three distinct material phases: air in the lumens, wood cell-wall and cured adhesive. This paper demonstrates a method for homogeneously tagging a resol, PF adhesive with iodine (I) to yield sufficient XCT contrast for quantitative material segmentation, with minimal phase overlap. Segmented, bondlines can yield novel and valuable 3D information about adhesive penetration within porous wood structures without damaging specimen joints. Method refinement and development involved the formulation and analysis of two preliminary PF resins, partially tagged with bromine (Br) and I.

2 Experimental

2.1 Adhesive formulation

Brominated (BrPF), iodinated (IPF1 and IPF2) and control PF resins (1000-2000 g) were prepared with assistance from Arclin, Springfield, Oregon to mimic conventional plywood resins. Meta-bromophenol and meta-iodophenol (98% purity) were included in the BrPF and IPF1 resins at phenol to X-phenol molar ratios of 14.3 and 5.0, respectively; meta-iodophenol accounted for the entire phenol component in IPF2. Formulations were prepared with formaldehyde to phenol-component molar ratios between 1.8 and 2.5 in the presence of a sodium hydroxide (NaOH) catalyst. Reaction temperatures were controlled between 40°C and 90°C over an 8 hour period; formulations were considered complete when resin viscosities were between 500 and 600 mPa·s at 25°C. Final adhesives (43% solids, pH ~11.5-12.5) were kept frozen (-10°C) between analyses and bonding.

2.2 Gel permeation and ion chromatography

Gel Permeation and Ion Chromotography (GPC and IC, respectively) analyses were conducted by Arclin according to their proprietary analytical procedures. GPC with a Viscotek Triple Detection SEC System and a bank of PLgel columns provided

adhesive absolute molecular weight and polydispersity. Analysis for bromide and iodide anions was accomplished with a HP1090 instrument equipped with a Shodex CD-4 detector and Hamilton PRP-100X column.

2.3 Powder density, neutron activation analysis, and x-ray radiography

Cured resin samples (1 - 3 g, 125°C, 3 h) were weighed for percent solids [25], and ground to a powder in a Wiley Mill (30 mesh, ≤ 0.595 mm). Powder densities were determined according to a modified version of ASTM D 5965, method A [26], where the immersion liquid was deionized water.

Br and I concentrations were verified from cured adhesive powder with Neutron Activation Analysis (NAA). BrPF and IPF1 samples (300 - 400 mg) were analyzed with epithermal neutrons at the McMaster Nuclear Reactor in Hamilton, Ontario, Canada, and induced radioactivity (^{80}Br – 617 KeV or ^{128}I – 443 KeV) was collected with a hyper-pure gamma-ray spectrometer. IPF2 samples (100 mg, n = 3) were analyzed with thermal neutrons using the TRIGA Mk. II Research Reactor at Oregon State University (OSU), Corvallis, Oregon; subsequent gamma radiation (^{128}I – 526.6 KeV) was collected with a HPGe detector. Calibration, at both facilities was achieved using appropriate sub-standards [27].

Adhesive x-ray adsorption contrast was observed as a function of iodine concentration with ground resin mixtures of IPF1 and a PF control. Polyethylene vials (20 mm tall x 9.5 mm diameter) were partially filled with the homogenized powder mixtures, which were tamped down to minimize void-space. Transmission, 2D radiographs of each vial were collected with polychromatic x-rays (25 kVp, 312 μA) on a cone-beam scanner in the School of Mechanical, Industrial and Manufacturing Engineering at OSU. The system consisted of a Feinfocus 160 kVp source and tungsten target, with a 9-inch image intensifier detector (Medelex HXS-93/PS). Digital gray-scale images were recorded with a 16-bit CCD camera (Point Grey, GRAS-5055M). A flat-field correction was applied to each radiograph using bright-field and dark-field projections [10]. Image processing and analyses were performed with the software package Fiji, which is based on ImageJ [28,29]. 'Flattened' projections were cropped to a 2 mm wide vertical column in the center of each vial. Mean gray-scale (transmitted intensity) values were compared for the largest possible areas of both pure air and pure resin powder within each column.

2.4 Composite specimen preparation

Single-bondline composite laminates were prepared from Douglas-fir (*Pseudotsuga menziesii*, DF), loblolly pine (*Pinus taeda*, SYP) or hybrid poplar (*Populus deltoides x Populus trichocarpa*, HP). Individual laminae were conditioned to approximately 12% moisture content and freshly-planed immediately prior to bonding. Adhesives were applied to laminae tangential-longitudinal planes with a steel roller at 120 g/m² based on resin solids, and bonded in a hot press (185 °C, 8 min,

689.5 kPa). Specimens (2 mm x 2 mm cross-section x 10 mm long) were carefully excised from each laminate using a bandsaw and razor-blade, such that they contained a central, longitudinal bondline.

2.5 Fluorescence and scanning electron microscopy (FM and SEM, respectively) and energy dispersive spectroscopy (EDS)

Composite specimens were embedded with Spurr Low-Viscosity ERL 4221 epoxy under a low vacuum [30,31] for easier surface preparation and to minimize charge build-up in empty cell lumens during SEM analysis. Ultra-smooth, cross-section surfaces were prepared with a Leica EM UC7 ultra microtome, and observed with a Nikon E400 epi-fluorescent microscope, equipped with a high pressure mercury lamp (100W) and UV (300-380 nm excitation "EX", 400 nm dichromatic mirror "DM", and 420 nm emission "EM") or blue-light (420-490 nm EX, 500 nm DM and 515 nm EM) filter sets [32,6]. Digital FM images were collected with a QImaging MicroPublisher 5.0 RTV CCD camera and QCapture Pro 5.1 image software. The same specimen surfaces were subsequently imaged on a FEI Quanta 3D SEM equipped with EDS after being sputter coated with a thin, conductive layer of a gold/palladium alloy. Elemental maps of carbon, oxygen, nitrogen, sodium, bromine, rubidium, iodine, chlorine, gold and palladium were collected over the same field of view as the FM images with the following parameters: image resolution 512x442 pixels, 16-32 nA beam current, 10-15 kV beam energy, 10.5 mm working distance, 64 frames per map, 200 µs dwell time, 20-30% dead time, which resulted in approximately 10K - 20K counts/s. Semi-quantitative EDS spectra (100 s) were also collected with the same instrumental parameters from two surface points on each specimen: an adhesive-filled lumen and a cell-wall not in contact with PF resin. Composite (overlaid) elemental maps of oxygen, and the tag element of interest (Br, I, Na or Rb), were prepared with the following processes in Fiji: 1) single element maps were converted from 8-bit color to grayscale images; 2) high intensity outlier pixels were removed with a 1 pixel radius; 3) mean 'background' pixel values were subtracted from all image points to remove low-intensity (noise); 4) resulting images were linearly normalized, with 0.4% saturation tolerance, to stretch the pixel intensities over the full 0 - 255 gray-scale range; 5) elemental maps were merged to form RGB composites, with the red and green color channels assigned to the oxygen and tag-signals, respectively.

2.6 Synchrotron, micro x-ray computed tomography (XCT)

XCT analyses were performed at two synchrotron bend-magnet facilities. BrPF and IPF2 composites were scanned on beamline 2-BM-B at the Advanced Photon Source (APS) at the Argonne National Laboratory, Argonne, Illinois. IPF1 specimens were imaged on beamline 8.3.2 at the Advanced Light Source (ALS) at Lawrence Berkeley National Laboratory, Berkeley, California. Experimental parameters are provided in Table 1. Both facilities used parallel Si(111) monochromators

to image at the specified energies, and LuAG scintillator materials to convert detection signals into visible light. Radiograph projections were then recorded with a 12-bit Roper Scientific CoolSnap K4 HQ CCD camera with 5X objective at the APS, and a 14-bit Cook PCO4000 CCD camera with 10X objective at the ALS. Tomograms from both sources were reconstructed with fast filtered back projection algorithms [33,10] and stored as stacks of floating-point gray-scale slices.

Table 1 XCT acquisition parameters for tagged-PF wood composites

Resin	Beam-line	Beam energy [KeV]	Rotation angle [°]	Projections	Exposure time [ms]	Sample to detector distance [mm]	Voxel side length [µm]	Reconstructed slices
Control & BrPF	APS 2-BM-B	14.05	0.12	1504	250	15	1.45	2047
IPF1	ALS 8.3.2	35	0.125	1441	3500	30	0.9	2569
IPF2	APS 2-BM-B	15.3	0.12	1504	250	8	1.45	2047

3 Results and Discussion

The three systems discussed in this work, BrPF, IPF1 and IPF2, illustrate the experimental progression undertaken to develop a PF adhesive capable of yielding high gray-scale contrast in micro-XCT images of bonded wood-composites. For comparative purposes, information is also provided for a PF adhesive containing rubidium (Rb), which was studied by Modzel and colleagues in 2009, hearafter referred to as RbPF. The RbPF adhesive did provide significantly enhanced micro XCT contrast to wood cell-walls [34,15]; however, the Rb was added as a RbOH catalyst in the PF formulation, in substitute of the more conventional catalyst, NaOH. Having not been directly bound to the PF polymer chains, Rb ions migrated independent of the adhesive penetration during bonding. This migration was proposed to have caused variations in localized Rb concentrations across composite joints, which helped explain contrast differences observed between specimens prepared and scanned under similar conditions [34].

In the present work, it was paramount to develop a system in which the tag-element was attached to the resin polymers. Yet, it is important to clarify that the adhesives presented here were not intended to represent the bonding behavior and properties of any particular commercially-relevant system. It was recognized that inclusion of contrast-agents, of any type or concentration, would undoubtedly influence adhesive properties, which already vary widely across different PF formulations [35,36]. The primary goal was to prepare a PF system which penetrated the wood upon bonding, transferred bondline stresses once cured, and could be successfully segmented in reconstructed XCT datasets; nevertheless, the presented systems were prepared based on conventional plywood resin formulations in terms of desired percent solids and viscosity. While BrPF,

IPF1 and IPF2 results are all provided together, note that the development of these systems included three separate experiments at synchrotron XCT sites (Table 1), with increasing success in tag efficacy and afforded image contrast. Figure 1 provides example XCT cross-section images of composite specimens bonded with each experimental adhesive; in each case, two sub-areas from the same reconstructed slice are provided with their corresponding gray-scale histograms. The first area shows only wood cells and empty lumens, while the second shows the bondline region with adhesive filled or coated lumens. Comparison of the histogram shapes within and between each specimen helps illustrate both the adhesive development and some of the image noise and artifacts encountered and overcame throughout this study.

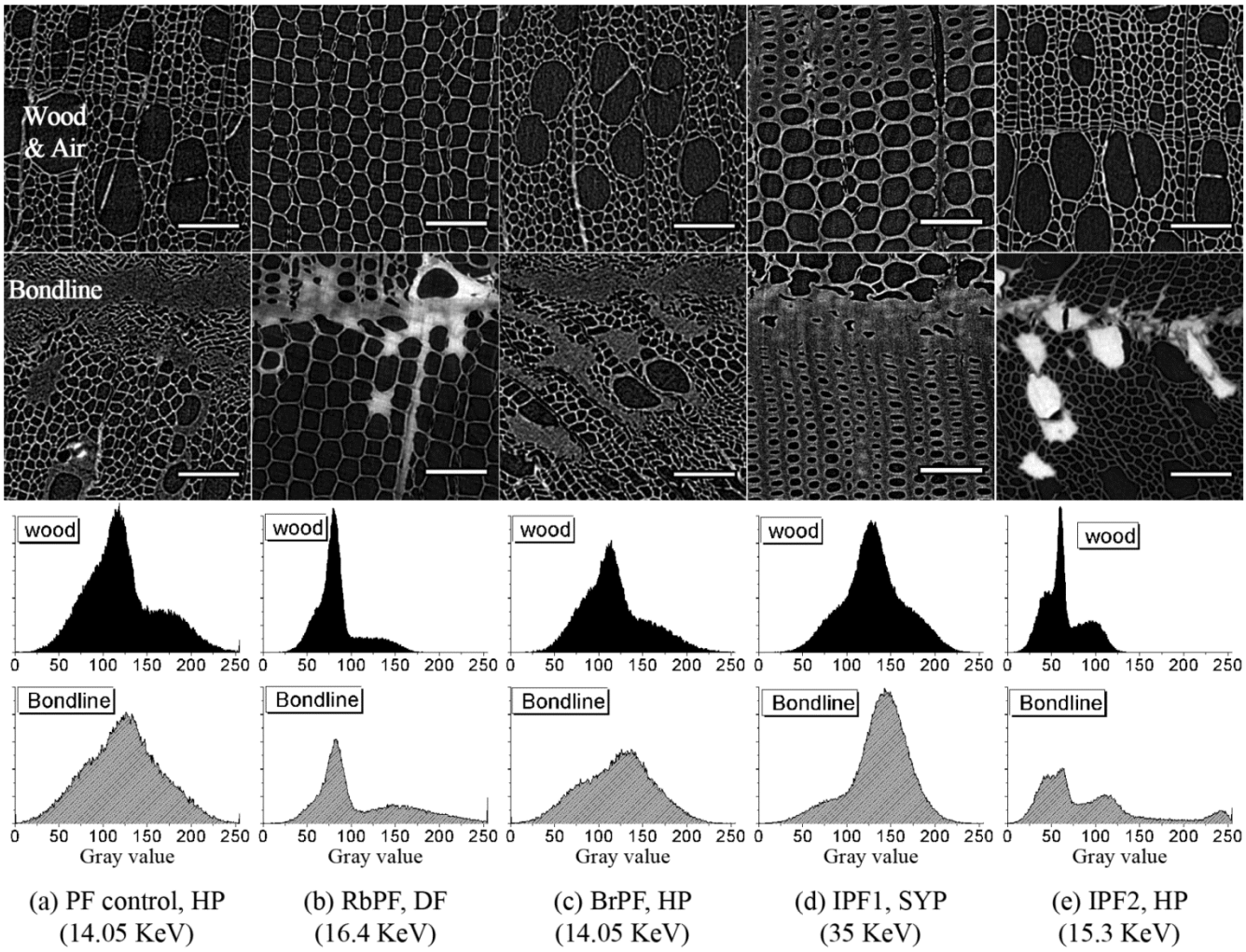

Fig. 1 Cross-section XCT slices of each specimen type with indicated scan energy. Sub-areas of wood and air only (top row), and region containing a horizontal bondline (bottom row) were selected from the same reconstructed image (scale bars = 100 μm). Parent images were first normalized to utilize the full 256 bit gray-scale range. Gray-scale histograms correspond to the respective sub-areas, and each histogram pair has the same area under the curve (vertical axis = pixel count)

Initially, Br was chosen as the tag element because it has similar atomic mass to Rb (Z_{Br} = 35, Z_{Rb} = 37), and meta-bromophenol has previously shown to support PF polymerization [37,38]. During the synthesis of PF resins, methylolation of phenol typically occurs at the ortho and para positions of the ring. The attachment of bromine at the meta position of the ring was not expected to prevent polymerization. The polymerization reaction progressed as expected; however, BrPF failed to yield any noticeable x-ray absorption contrast in the bonded specimens (Figure 1c, bottom). APS beamline scientists suggested iodine might be a more effective contrast agent, as it is significantly heavier than bromine (Z_I = 53). Thus, IPF1 was prepared using meta-iodophenol and at a higher molar ratio to un-substituted phenol, effectively increasing the tag mass and concentration from the BrPF resin. Yet, IPF1 XCT data suffered from increased image noise, and yielded limited and inconsistent contrast between the wood and adhesive phases. Moreover, in a few instances, adhesive occupying lumens far from the bondline appeared brighter than adhesive directly at the joint interface (Figure 1d, bondline). It was suspected that during formulation the phenol and I-tagged phenol reactants likely polymerized at different rates, were incorporated into different chain lengths, and perhaps yielded different degrees of branching and cross-linking. Certainly, one would expect the mobility and reactivity of a halogen-substituted phenol to be different relative to an un-substituted phenol. Consequently Br and I distributions on the PF adhesive chains were likely heterogeneous, which resulted in different localized tag concentrations in bonded joints. The third adhesive, IPF2, was formulated entirely with meta-iodophenol to ensure uniform iodine distribution across all PF polymers, independent of molecular weight or morphology. This also significantly raised the overall wt% I in the cured resin. IPF2 did provide sufficient XCT image contrast for 3D material segmentation, as depicted in Figure 2. This paper details the properties of each resin, and why IPF2 was successful compared to the first two trials.

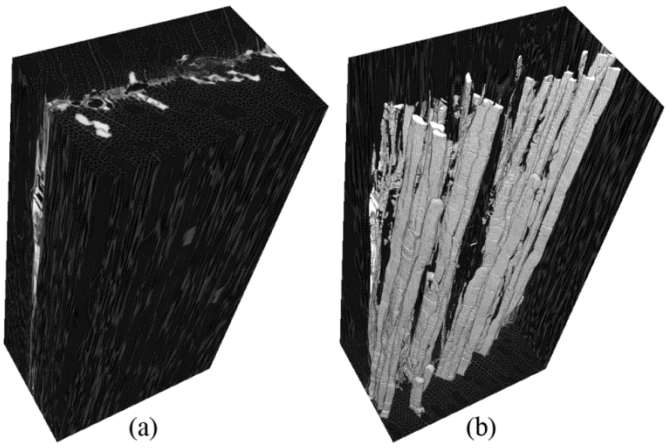

Fig. 2 XCT sub-volume (1.71 mm^3) virtually excised from the same HP, IPF2 specimen in Figure 1e. (a) Solid 3D volume; (b) segmented, adhesive phase not including the wood material occupying the same internal space

3.1 Adhesive properties

Table 2 provides the collective physical properties and tag concentrations for each experimental PF adhesive. Viscosity and molecular weight were measured just after formulation, while density and percent solids were measured from cured samples of each adhesive, with the exception of RbPF; its percent solids, molecular weight and viscosity were reported elsewhere [34]. The RbPF density of 1.3 g/cm³ was assigned as a conservative estimate, which neglected any added Rb mass, but was in the typical range of cured PF adhesives [36,39]. Tag concentrations were first predicted for each adhesive using the percent solids value and known formulation reactant quantities [34], and then measured directly with NAA. Each system resulted in similar solids content and viscosity, as intended. Molecular weight increased with tag mass and quantity; however, each system had a similar polydispersity index (PDI), or ratio between weight average and number average molecular weights. IPF1 was the only exception, with slightly lower viscosity and PDI; its viscosity was expected to advance slightly between formulation and bonding. Curiously, BrPF had a noticeably reduced powder density than the control PF. Perhaps the meta-Br presence resulted in the formation of more linear polymer chains with lower potential cross-linking than the un-substituted PF morphologies; in turn, this may have reduced the polymer packing efficiency upon resin cure. The higher GPC Mark-Houink coefficients of the BrPF and IPF resins relative to the control lend credence to this view. The added void-volume may have offset the added mass from the heavier Br atoms, which were, after all, only present at 3.3 wt% in that system. Similar, polymer morphologies likely formed in the IPF1 and IPF2 resins, though the higher tag concentrations and masses were able to overcome any excess void-volume effects, and thus increase the overall cured density in these systems. In each resin, the calculated and measured concentrations agreed very closely, indicating that little to no tag material was liberated during formulation or cure.

Table 2 Adhesive material properties. Molecular weight data includes number average (Mn), weight average (Mw) and PDI (Mw:Mn). Standard deviation in parentheses (n=3). BrPF and IPF NAA results are from a single replicate. RbPF results were adopted from another report [34]; RbPF density was estimated

Adhesive	Solids	Powder density	Viscosity	Molecular weight			Cured resin tag concentration	
	[%]	[g/cm³]	[mPa·s]	Mn	Mw	PDI	Calculated [wt%]	Measured [wt%]
Control PF	43.2	1.43 (0.06)	600	3110	5920	1.90	-	-
BrPF	43.8	1.28 (0.06)	700	9180	16570	1.81	3.3	3.2
IPF1	44.0	1.57 (0.03)	515	14420	16360	1.13	12.1	12.2
IPF2	44.1	2.24 (0.06)	600	11800	22380	1.90	41.1	39.5 (0.2)
RbPF	47.0	1.3	750	1987	-	-	25.7	-

3.2 Adhesive x-ray attenuation

X-ray absorption contrast depends on the relative difference in linear attenuation coefficient, μ, between neighboring materials; in turn, μ depends on material density and molecular formula [22]. To better understand why the RbPF system yielded good contrast, and to explain the results of the presented experimental resins, theoretical attenuation length was determined for each adhesive [40]. Attenuation length describes the depth an incident photon will penetrate into a material before its probability of being absorbed or scattered becomes 1/e; μ is the inverse of attenuation length with units of reciprocal distance [22]. Theoretical attenuation lengths were calculated for the various materials in the XCT wood-composite specimens; observed differences in the theoretical μ values were expected correlate with and elucidate observed gray-scale contrasts. Cellobiose was chosen to represent wood cell-wall polymers, and was assigned a density equal to that of the cell-wall substance, approximately 1.54 g/cm³. Figure 3a shows a representative cellobiose repeat unit. Cured adhesive formulae were calculated using the known formulation reactants and quantities, the measured solids content, and a theoretical PF dimer repeat-unit. Figure 3b shows two phenol units which were first fully methylolated at the para and ortho positions, then polymerized linearly via a dimethylene ether linkage, common for resol-type PF adhesives at synthesis temperatures below 150°C [41,42,35]. While it is likely that different morphologies also formed during polymerization and cure, this structure was assumed a good approximation for the attenuation calculation. IPF2 provided an opportunity to check this assumption, as each phenol unit should have exactly one iodine substituent. Accordingly, the IPF2 molecular formula based on the provided structure should have an iodine stoichiometric coefficient of two. The calculated iodine coefficient was 1.85, which was determined sufficiently close to mass balance considering the calculation contained additional variability in the solids and reagent quantities.

Figure 3c is a plot of log attenuation coefficient as a function of beam energy; the figure key provides the density and molecular formula used for each material in the calculation [40]. Cellobiose attenuation closely matched theoretical wood results presented elsewhere [13]. It is clear that with similar molecular formulae and density there is no discernible difference in attenuation between the control PF and cellobiose within the provided photon energy range. As a result, XCT reconstructions of wood-composites bonded with control PF adhesives failed to provide enough image contrast for material segmentation (Figure 1a, bondline). Just above the Rb k-shell electron binding energy (k-edge = 15.3 KeV), the calculated RbPF attenuation coefficient is 24 times greater than for cellobiose. RbPF yielded sufficient image contrast (Figure 1b, bondline) in this energy range, yet quantitative segmentation suffered from tag mobility complications [34]. BrPF, scanned just above the Br k-edge (13.7 KeV), yielded a theoretical attenuation coefficient only three and a half times more than cellobiose; this clearly was not enough for sufficient contrast (Figure 1c, bottom). The predicted IPF1 attenuation is about

seven times greater than for cellobiose within the range studied; however, IPF1 specimens were scanned above the I k-edge (33.2 KeV), which was beyond the attenuation calculation range [40]. Nevertheless, a sharp increase in attenuation was expected above the k-edge, similar to the Br and Rb species. However, the increased energy also significantly reduced the cellobiose attenuation, which increased image noise.

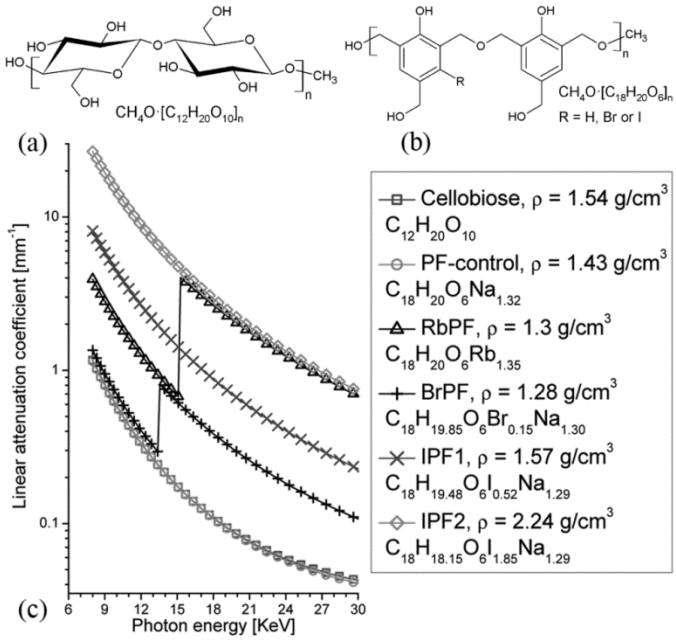

Fig. 3 Repeat units and molecular formulae for (a) cellobiose and (b) cured resol-PF adhesive polymers used to calculate theoretical attenuation coefficients for each material as a function of beam energy (c); plot key indicates specific molecular formulae and density values used for each attenuation prediction

Scintillator detectors assign photon intensities to specific gray levels ranging from pure black to pure white, with a floating point value. Quantitative phase segmentation with simple gray-scale threshold operations requires clearly defined valleys between material peaks; furthermore, segmentation confidence increases with decreasing peak overlap. The bondline histograms in Figure 1 illustrate this concept. Composite specimen b exhibits two clear peaks, which can be segmented with a threshold centered in the valley separating them; for specimen e, three material phases could be quantitatively segmented as there are two clear valleys (Figure 1). Image processing procedures, such as edge-preserving median filters, can further decrease phase overlap and improve segmentation confidence [12,19,43,20]; however, some initial contrast is still necessary. Wood-based composites contain three separate material phases, air, wood and adhesive; an optimal histogram for quantitative segmentation would thus consist of three isolated peaks distributed along the gray-scale range, as observed in Figure 1e. Peak height represents pixel count for a particular gray value, while peak breadth relates to how confidently one can assign a peak to a particular material. Broader peaks represent low signal-to-noise levels and/or overlaps in material gray values. The tallest

peak in each histogram represents air; the brighter peak (high gray-scale value), or shoulder when there is little contrast, immediately to the right of the air peak represents wood cell-walls. The darker peak (low gray-scale value), or shoulder, left of the air peak is an artifact caused by large differences in density and refractive index at the interface of dissimilar materials [34,44,10]. With a fixed gray-scale range, simply maximizing the attenuation difference between any two phases could reduce the achievable contrast for the third. For example, Figure 1d shows the greatest overlap between the air and wood peaks, and these specimens were scanned at the highest energy.

X-ray radiographs of control PF and IPF1 adhesive powders were collected to determine if absorption contrast could be enhanced with increasing wt% I, even below the iodine k-edge. Figure 4 compares the mean gray-scale pixel intensity from regions containing air-space and ground resin in each projection image. Note that the response variable in this figure is transmission intensity, which is opposite from XCT gray-scale intensity. In radiographic projections, high pixel intensities correspond with high photon transmission through the material (i.e. low absorption); with XCT high pixel intensities relate to high attenuation (i.e. low transmission). Air intensity was uniform in each projection, while adhesive transmission intensity decreased significantly from zero to 12.2 wt% I. Bulk, or apparent, density (ρ_{bulk}) was checked as a confounding factor since x-ray attenuation is influenced by density and composition [22]. The void volume fraction (υ_a) in the powder column is inversely proportional to ρ_{bulk}. Despite cured IPF1 being denser than control PF, ρ_{bulk} and υ_a did not correlate with the observed intensity behavior (Figure 4).

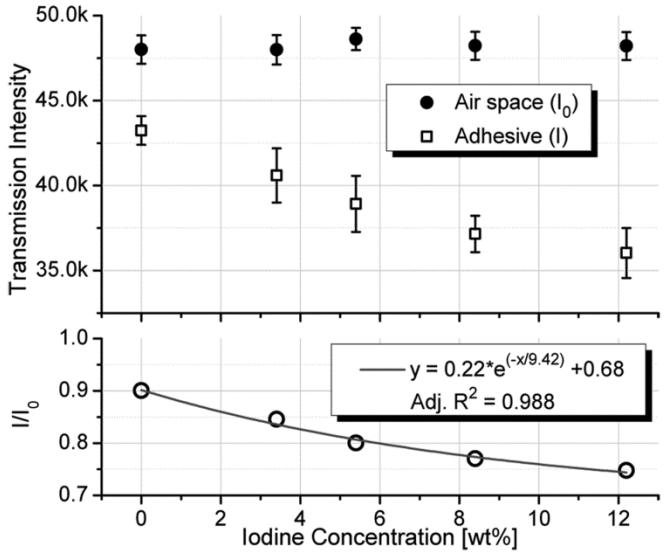

wt% I	0.0	3.4	5.4	8.4	12.2
ρ_{bulk} [g/cm³]	0.71	0.61	0.59	0.58	0.54
ν_a	46.0	57.5	56.8	61.1	63.4

Fig. 4 (top) Mean x-ray transmission (gray-scale) intensity through air and adhesive powder with increasing wt% iodine, error bars indicate $\pm$ 1 standard deviation; (bottom) mean intensity ratio, I/I_0, and fitted regression line; measured wt% I, apparent densities and void-volume fractions are also provided

In both air-space and adhesive filled regions, the transmitted x-rays passed through both container walls and the internal material. The relationship between adhesive intensity (I) and airspace intensity (I_0) was expected to follow the Beer-Lambert attenuation law, and an exponential fit to the ratio data showed a high adjusted R^2 of 0.988. The significance of the relationship showed that even below the iodine k-edge, and independent of bulk density, increasing iodine concentration would further reduce transmission intensity, resulting in greater XCT contrast.

IPF2 was prepared based on the results from both BrPF and IPF1. Meta-iodophenol made up the entire phenol component in IPF2, to maximize the achievable iodine concentration with the presented method and ensure all resin polymers were substituted to the same degree, regardless of chain length. Cured IPF2 contained 39.9 wt% I, and had a density of 2.24 g/cm^3 (Table 2). Accordingly, IPF2 showed the highest theoretical attenuation of all adhesives including RbPF (Figure 3c). Subsequent XCT data, collected below the iodine k-edge, yielded significantly enhanced adhesive contrast. The bondline image in Figure 1e shows dark void spaces in empty lumens, light-gray cell-walls and bright adhesive at the bond interface and in several vessels; these phases correspond to the three primary peaks in the IPF2 bondline histogram. Also, the IPF2 adhesive gray value is more consistent than the other systems, as evident by the clear, rightmost peak in the bondline histogram (Figure 1e). This observation is intuitive because all IPF2 polymer chains contained the same degree of iodine substitution. In Figure 1b, RbPF appears less consistent; the brightest regions likely indicate higher Rb concentrations [34]. Consequently, the RbPF bondline histogram shows no clear distinction between wood and adhesive peaks; rather, they form one broad peak which extends farther along the gray-scale range than the shoulder in the wood-only histogram. As was the case, RbPF could not be segmented. The IPF2 system, however, was segmented (Figure 2) with gray-scale thresholds in the valleys between each peak.

The above results indicate that density, molecular formula, tag uniformity and signal-to-noise ratio all impact adhesive x-ray contrast. Wood and adhesives are complex, organic systems with similar density; x-ray absorption contrast between the two materials requires ample difference in attenuation coefficients. Perhaps, an adhesive consisting entirely of meta-bromophenol would achieve similar results as IPF2 if it were scanned just above the Br k-edge; however, its density would likely be lower than IPF2. Similarly, one might argue that contrast might be even greater for IPF2 if it were imaged above the I k-edge; yet, this would increase image noise since beam attenuation in wood is drastically decreased at such high beam energies.

3.3 Tag mobility assessment

Quantitative segmentation of a tagged adhesive requires the contrast agent to remain attached and uniformly distributed along the polymers throughout both the formulation and bonding processes. Initially, there was concern that the Br and I tags, attached at the meta position of the phenol reactants, might be released from the aromatic rings when exposed to the high temperature and pH reaction environments during adhesive cook. However, IC results showed no free bromide or iodide ions in any of the experimental adhesives following formulation. Composite specimens were bonded at still higher temperatures than formulation. NAA results confirmed that resin powders contained the same tag concentrations as predicted (Table 2); yet, it was unclear whether the Br and I were, in fact, still attached to the cured PF polymers. Fluorescent micrographs and EDS elemental maps were used to determine if observed adhesive locations corresponded with tag spectra. Figure 5 compares the FM and EDS images from the same surfaces of specimens bonded with each resin. In each FM image, dark PF adhesive shows clear contrast to surrounding, light-colored cells. In EDS images, the oxygen elemental signal, shown in red, most clearly represented the wood structure, as the embedding epoxy had a lower oxygen concentration than the surrounding cell-walls. Tag-element maps, shown in green, are overlain on the oxygen maps. EDS spectra include the cumulative detected fluorescent counts from 64 scans for each element of interest. Raw images exhibited a uniform level of background noise from low intensity pixels only detected in a single or few scans; however, this was easily removed with simple image processing.

Figure 5b shows Rb contamination in cell-walls far from the RbPF specimen bondline and around cell lumens void of adhesive; this supports earlier evidence that the Rb ions moved independent of the adhesive polymers [34,15]. The EDS images of BrPF, IPF1 and IPF2 (Figures 4d, f and h, respectively) show tag signals directly correspond with the adhesive locations in the matching FM images. For BrPF and IPF1, only a portion of the phenol reactants were substituted. Tag concentration in these systems were likely heterogeneous across different polymer molecular weight, and thus polymer mobility was effected; this might explain the observed non-uniformity in tag-signal intensity. However, iodine intensity in IPF2 appears consistent at all adhesive locations. Additionally, semi-quantitative point spectra of the Br and I-tagged composite specimens showed there were no measurable traces of tags on cell-wall edges far from the bondline and not in contact with adhesive.

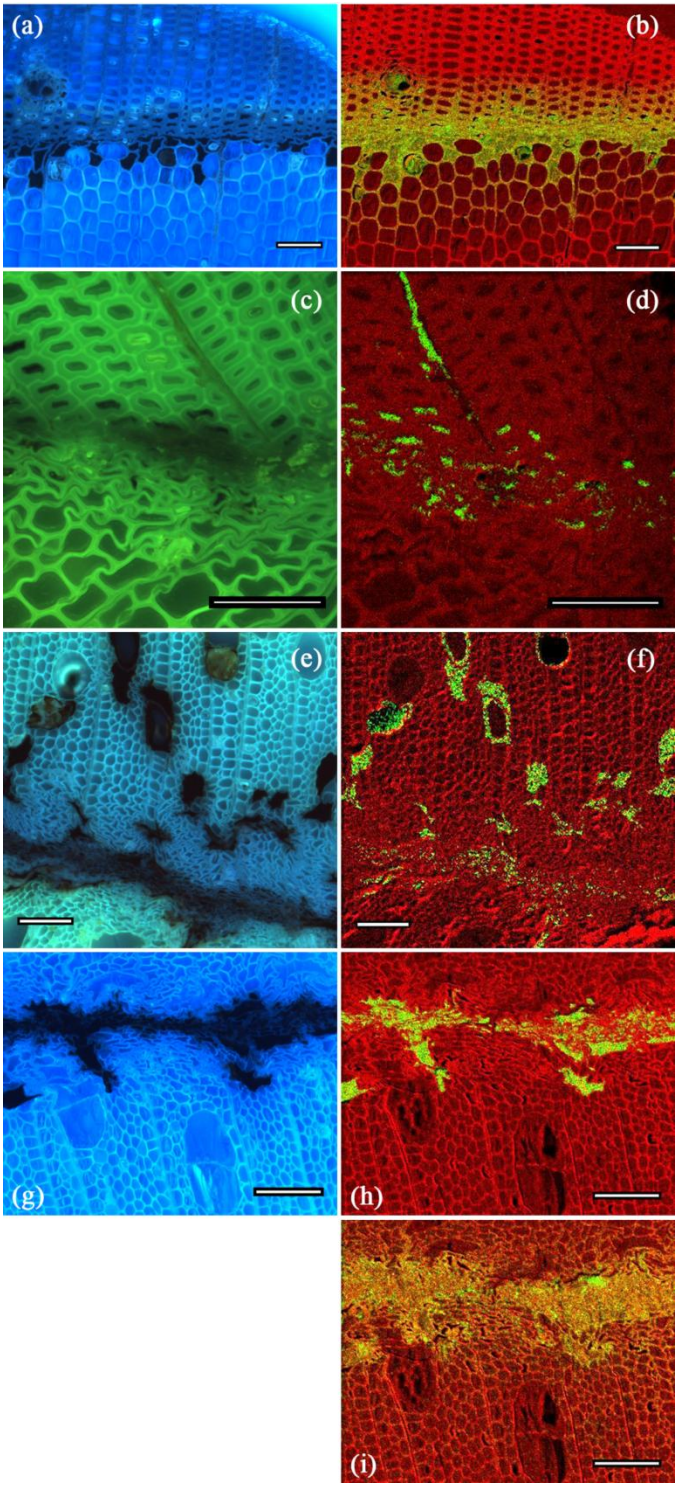

Fig. 5 FM images (left) and EDS elemental maps (right) of the same specimen surface for composites bonded with RbPF (a & b, DF), BrPF (c & d, SYP), IPF1 (e & f, HP) and IPF2 (g - i, HP). BrPF FM image (c) acquired with 'blue' filterset and (a , e & g) aquired with UV filterset. EDS red phase represents oxygen signal and green indicates tag-element of interest: Rb (b), Br (d), I (f & h) and Na (i). Scale bars = 100 μm **(Reproduce in color)**

Rb ions were included as an alkaline catalyst during the RbPF adhesive formulation [15]; the conventional catalyst system, NaOH was used in formulation of the BrPF and IPF resins. Figure 5i shows the Na elemental map for the IPF2 specimen. As with Rb (Figure 5b), the Na signal intensity appears non-uniform in the bondline region, and Na ions migrated far from the bond interface. However, unlike the Rb ions, sodium appeared indiscriminately in both cell-walls and epoxy-filled lumens. This is not surprising as Na is much smaller and more reactive than Rb, affording it greater mobility. Na ions distributed throughout the wood cells after adhesive cure were likely remobilized by the liquid epoxy embedding media before it hardened. Several studies have shown similar migration and agglomeration behavior for ions or metal-particles dispersed in liquids designed to penetrate wood structures [9,13,23,24,45,46]. Often wood's heterogeneous chemical and anatomical structures magnify these separation effects. Charged ions may be preferentially absorbed into different cell-wall layers, and micro- or nano-sized metallic particles can often be size excluded from penetration by small pit structures [45,46]. Therefore, if contrast agents are required to quantify the penetration behavior of an adhesive or solution into wood structures, consideration must be given to chemical or physical phase separation.

The collective IC and EDS results indicate that the halogen substituents remained attached to the phenol reactants throughout formulation and bonding. Furthermore, the IPF2 tag concentration appeared uniform across the polymer molecular weight distribution, since it consisted entirely of meta-iodophenol; this observation is consistent with the uniform XCT gray-scale intensity in Figure 1e. It is true that one would not expect a PF resin prepared with a substituted phenol to polymerize in the same manner as one containing only phenol. However, the goal of this work was to develop an adhesive system which could be confidently segmented from wood-composite XCT data. The BrPF and IPF adhesives presented here were formulated according to one particular recipe. This of course could be adjusted for different desired molecular weight distribution, viscosity, solids content or cross-linking potential, all of which in turn would affect adhesive penetration and performance behavior.

4 Conclusions

A resol-type, phenol formaldehyde adhesive formulated with meta-iodophenol yielded sufficient and consistent micro x-ray computed tomography image contrast in bonded wood-composites. Air, wood and adhesive phases could all be segmented from reconstructed 3D datasets with simple histogram thresholds centered between the three material gray-scale peaks. Preliminary adhesives containing lower concentrations of iodine or bromine were also presented and compared with a control and rubidium-labeled adhesive. X-ray absorption contrast improved with increasing tag mass and concentration and cured adhesive density; however, image quality and segmentation confidence suffered at high beam energies when signal-to-noise levels were low. X-ray results for wood and adhesives agreed with theoretical attenuation behavior predicted for each

material as a function of beam energy. Tag efficacy and mobility were also accessed with multiple chemical and visual analyses including ion chromatography, neutron activation analysis, fluorescent microscopy and energy dispersion spectrometry. The iodine and bromine tags, originally covalently bonded to the formulation reactants, remained associated with the liquid and cured adhesive polymers. Sodium and rubidium, which were merely mixed into the liquid adhesives as polymerization catalysts, retained high mobility, and migrated independent of the adhesive polymers during bonding. The presented formulation could be modified to achieve different viscosity, solids content, or molecular weight distribution, which would in turn influence penetration behavior and joint performance. The afforded x-ray tomography contrast and segmentation confidence with these tagged adhesives can help improve fundamental understanding of wood adhesion and the role of adhesive penetration.

ACKNOWLEDGEMENTS

Use of the Advanced Photon Source was supported by the U. S. Department of Energy, Office of Science, Office of Basic Energy Sciences, under Contract No. DE-AC02-06CH11357.The Advanced Light Source is supported by the Director, Office of Science, Office of Basic Energy Sciences, of the U.S. Department of Energy under Contract No. DE-AC02-05CH11231. Financial support was provided by the Wood-Based Composites Center, a National Science Foundation Industry/University Cooperative Research Center. Resin formulation and technical assistance were provided by Arclin, in Springfield, Oregon.

REFERENCES

1. Pocius AV (1997) Adhesion and adhesives technology: an introduction. Hanser Publishers; Hanser/Gardner Publications, Munich, New York; Cincinnati, Ohio
2. Schultz J, Nardin M (1994) Theories and mechanisms of wood adhesion. In: Pizzi A, Mittal KL (eds) Handbook of Adhesive Technology. Marcel Dekker, Inc., New York, pp 19-33
3. Ebewele RO, River BH, Koutsky JA (1982) Relationship between phenolic adhesive chemistry, cure and joint performance .part I. Effects of base resin constitution and hardener on fracture energy and thermal effects during cure. Journal of Adhesion 14 (3-4):189-217
4. White MS (1977) Influence of resin penetration on the fracture toughness of wood adhesive bonds. Wood Science 10 (1):6-14
5. Frazier CE, Ni JW (1998) On the occurrence of network interpenetration in the wood-isocyanate adhesive interphase. International Journal of Adhesion and Adhesives 18 (2):81-87
6. Kamke FA, Lee JN (2007) Adhesive penetration in wood - a review. Wood and Fiber Science 39 (2):205-220
7. Banhart J (2008) Radiation sources and interaction of radiation with matter. In: Banhart J (ed) Advanced Tomographic Methods in Materials Research and Engineering. Oxford University Press, Oxford, New York, pp 107-140
8. Banhart J (2008) Introduction. In: Banhart J (ed) Advanced Tomographic Methods in Materials Research and Engineering. Oxford University Press, Oxford, New York, pp 3-18
9. De Vetter L, Cnudde V, Masschaele B, Jacobs PJS, Van Acker J (2006) Detection and distribution analysis of organosilicon compounds in wood by means of SEM-EDX and micro-CT. Mater Charact 56 (1):39-48. doi:10.1016/j.matchar.2005.09.007
10. Haibel A (2008) Synchrotron x-ray absorption tomography. In: Banhart J (ed) Advanced Tomographic Methods in Materials Research and Engineering. Oxford University Press, Oxford, New York, pp 141-160
11. Hass P, Wittel F, Mendoza M, Herrmann H, Niemz P (2011) Adhesive penetration in beech wood: experiments. Wood Science and Technology:1-14. doi:10.1007/s00226-011-0410-6
12. Hass P, Wittel FK, McDonald SA, Marone F, Stampanoni M, Herrmann HJ, Niemz P (2010) Pore space analysis of beech wood: The vessel network. Holzforschung 64 (5):639-644. doi:10.1515/hf.2010.103
13. Mannes D, Marone F, Lehmann E, Stampanoni M, Niemz P (2010) Application areas of synchrotron radiation tomographic microscopy for wood research. Wood Science and Technology 44 (1):67-84. doi:10.1007/s00226-009-0257-2
14. Mannes D, Niemz P, Lehmann E (2009) Tomographic investigations of wood from macroscopic to microscopic scale. Wood Research 54 (3):33-44
15. Modzel G, Kamke FA, De Carlo F (2010) Comparative analysis of a wood:adhesive bondline. Wood Science Technology:12. doi:10.1007/100226-010-0304-z
16. Evans PD, Morrison O, Senden TJ, Vollmer S, Roberts RJ, Limaye A, Arns CH, Averdunk H, Lowe A, Knackstedt MA (2010) Visualization and numerical analysis of adhesive distribution in particleboard

using X-ray micro-computed tomography. International Journal of Adhesion and Adhesives 30 (8):754-762. doi:10.1016/j.ijadhadh.2010.08.001
17. Bucur V (2003) Techniques for high resolution imaging of wood structure: a review. Measurement Science & Technology 14 (12):R91-R98
18. Forsberg F, Sjodahl M, Mooser R, Hack E, Wyss P (2010) Full three-dimensional strain measurements on wood exposed to three-point bending: Analysis by use of digital volume correlation applied to synchrotron radiation micro-computed tomography image data. Strain 46 (1):47-60
19. Mayo SC, Chen F, Evans R (2010) Micron-scale 3D imaging of wood and plant microstructure using high-resolution X-ray phase-contrast microtomography. Journal of Structural Biology 171 (2):182-188. doi:DOI: 10.1016/j.jsb.2010.04.001
20. Trtik P, Dual J, Keunecke D, Mannes D, Niemz P, Stähli P, Kaestner A, Groso A, Stampanoni M (2007) 3D imaging of microstructure of spruce wood. Journal of Structural Biology 159 (1):46-55. doi:DOI: 10.1016/j.jsb.2007.02.003
21. Wildenschild D, Hopmans JW, Vaz CMP, Rivers ML, Rikard D, Christensen BSB (2002) Using X-ray computed tomography in hydrology: systems, resolutions, and limitations. Journal of Hydrology 267 (3-4):285-297. doi:10.1016/s0022-1694(02)00157-9
22. Ketcham RA, Carlson WD (2001) Acquisition, optimization and interpretation of X-ray computed tomographic imagery: applications to the geosciences. Computers & Geosciences 27 (4):381-400. doi:10.1016/s0098-3004(00)00116-3
23. Walther T, Thoemen H (2009) Synchrotron X-ray microtomography and 3D image analysis of medium density fiberboard (MDF). Holzforschung 63 (5):581-587. doi:10.1515/hf.2009.093
24. Wang Y, Muszyński L, Simonsen J (2007) Gold as an X-ray CT scanning contrast agent: Effect on the mechanical properties of wood plastic composites. Holzforschung 61 (6):723-730. doi:10.1515/hf.2007.117
25. ASTM-D-4426 (2006) Standard test method for determination of percent nonvolatile content of liquid phenolic resins used for wood laminating. vol ASTM D 4426-01. ASTM International, West Conshohocken, PA
26. ASTM-D-5965 (2007) Standard test method for specific gravity of coating powders. vol ASTM B 5965 - 02. ASTM International, West Conshohocken, PA
27. Minc LD (2008) Neutron Activation Analysis. Encyclopedia of Archaeology. Academic Press, New York
28. Schindelin J, Arganda-Carreras I, Frise E, Kaynig V, Longair M, Pietzsch T, Preibisch S, Rueden C, Saalfeld S, Schmid B (2012) Fiji: an open-source platform for biological-image analysis. Nature Methods 9 (7):676-682
29. Rasband WS (1997 - 2012) ImageJ.
30. Spurr AR (1969) A low-viscosity epoxy resin embedding medium for electron microscopy. Journal of ultrastructure research 26:31-43
31. Ellis E (2006) Solutions to the problem of substitution of ERL 4221 for vinyl cyclohexene dioxide in Spurr low viscosity embedding formulations. Microscopy Today 14 (4):32-33
32. Davidson MW, Abramowitz M (2002) Optical Microscopy. In: Encyclopedia of Imaging Science and Technology. John Wiley & Sons, Inc. doi:10.1002/0471443395.img074
33. Dowd BA, Campbell GH, Marr RB, Nagarkar VV, Tipnis SV, Axe L, Siddons DP (1999) Developments in synchrotron x-ray computed microtomography at the National Synchrotron Light Source.224-236. doi:10.1117/12.363725
34. Modzel G (2009) Computed X-ray analysis of wood-adhesive bonds. Dissertation, Oregon State University, Corvallis, OR
35. Pizzi A (2003) Phenolic resin adhesives. In: Pizzi A, Mittal KL (eds) Handbook of Adhesive Technology. Second edn. Marcel Dekker, Inc., New York,

36. Sellers T (1994) Adhesives in the wood industry. In: Pizzi A, Mittal KL (eds) Handbook of Adhesive Technology. Marcel Dekker, Inc., New York, pp 599-614
37. Smith L, Côté W (1971) Studies of penetration of phenol-formaldehyde resin into wood cell walls with the SEM and Energy-Dispersive X-ray Analyzer. Wood and Fiber Science 3 (1):56-57
38. White MS, Ifju G, Johnson JA (1977) Method for measuring resin penetration into wood. Forest Products Journal 27 (7):3
39. Umemura K, Takahashi A, Kawai S (1998) Durability of isocyanate resin adhesives for wood - I: Thermal properties of isocyanate resin cured with water. Journal of Wood Science 44 (3):204-210
40. Henke BL, Gullikson EM, Davis JC (1993) X-ray interactions - photoabsorption, scattering, transmission, and reflection at E=50-30,000 EV, Z=1-92. Atom Data Nucl Data Tables 54 (2):181-342
41. Frihart CR (2005) Wood adhesion and adhesives. In: Rowell RM (ed) Handbook of Wood Chemistry and Wood Composites. Taylor & Francis Group, New York,
42. Park B-D, Riedl B, Yoon Soo K, So WT (2002) Effect of synthesis parameters on thermal behavior of phenol–formaldehyde resol resin. Journal of Applied Polymer Science 83 (7):1415-1424. doi:10.1002/app.2302
43. Standfest G, Kutnar A, Plank B, Petutschnigg A, Kamke F, Dunky M (2012) Microstructure of viscoelastic thermal compressed (VTC) wood using computed microtomography. Wood Science and Technology. doi:10.1007/s00226-012-0496-5
44. Betz O, Wegst U, Weide D, Heethoff M, Helfen L, Lee WK, Cloetens P (2007) Imaging applications of synchrotron X-ray phase-contrast microtomography in biological morphology and biomaterials science. 1. General aspects of the technique and its advantages in the analysis of millimetre-sized arthropod structure. J Microsc-Oxf 227 (1):51-71
45. Matsunaga H, Kiguchi M, Evans PD (2009) Microdistribution of copper-carbonate and iron oxide nanoparticles in treated wood. Journal of Nanoparticle Research 11 (5):1087-1098. doi:10.1007/s11051-008-9512-y
46. Matsunaga H, Matsumura J, Oda K (2004) X-ray microanalysis using thin sections of preservative-treated wood - Relationship of wood anatomical features to the distribution of copper. Iawa Journal 25 (1):79-90